PHYSICAL REVIEW B **110**, 075425 (2024)

Higher-order topology in Fibonacci quasicrystals

Chaozhi Ouyang,[1,2] Qinghua He,[1,2] Dong-Hui Xu,[3,*] and Feng Liu[1,2,4,†]
[1]*Institute of High Pressure Physics, Ningbo University, Ningbo, 315-211, China*
[2]*School of Physical Science and Technology, Ningbo University, Ningbo, 315-211, China*
[3]*Deparment of Physics & Chongqing Key Laboratory for Strongly Coupled Physics, Chongqing University, Chongqing 400044, China*
[4]*Department of Nanotechnology for Sustainable Energy, School of Science and Technology, Kwansei Gakuin University, Gakuen 2-1, Sanda 669-1337, Japan*

(Received 26 January 2024; revised 26 June 2024; accepted 7 August 2024; published 21 August 2024)

In crystalline systems, higher-order topology, characterized by topological states of codimension greater than one, usually arises from the mismatch between Wannier centers and atomic sites, leading to filling anomalies. However, this phenomenon is less understood in aperiodic systems, such as quasicrystals, where bulk Wannier centers are absent. In this study, we examine a modification of Fibonacci chains and squares derived from a typical higher-order topological model, the two-dimensional Su-Schrieffer-Heeger model, to investigate their higher-order topological properties. We discover that topological interfacial states, including corner states, can emerge at the interfaces between modified Fibonacci chains and squares derived from topologically distinct parent systems. These interfacial states can be characterized by a shift in the local Wannier center spectrum, which indicates filling anomalies in finite samples. We numerically validate these interfacial states using the finite element method in phononic and photonic Fibonacci quasicrystals. Our results provide insight into the higher-order topology of quasicrystals and open avenues for exploring novel topological phases in aperiodic structures.

DOI: 10.1103/PhysRevB.110.075425

I. INTRODUCTION

Over the past two decades, the concept of topology has become a cornerstone in classifying solid-state materials, revealing essential differences even for materials with seemingly identical energy-band structures. Heralded by the topological band theory, this paradigm shift has profoundly reshaped our understanding of solid-state physics [1–3]. One of the most striking properties of topological band theory is the bulk-edge correspondence, connecting the bulk topological invariant in crystalline systems to the emergence of robust interfacial states in finite, topologically distinct samples [4–8]. In this evolving landscape, the exploration of higher-order topological phases, which deviate from conventional topological insulators by exhibiting bulk-corner correspondence, has gained prominence in recent years. These higher-order topological phases allow topological states of codimension greater than one, such as corner states, with potential applications in topological lasers and quantum computing [9–19].

Significant progress has been made in understanding higher-order topological states in crystalline systems, as evidenced by a wealth of studies. These studies could be exemplified by several models based on filling anomalies induced by mismatches between Wannier centers and atomic sites [20–24]. Protected by various symmetries [25–29], such as point group symmetry [30–32], inversion symmetry [33], and chiral symmetry [34,35], higher-order topological states are observed not only in solid-state materials [36–42], but also in metamaterials, such as photonic [43–48], sonic crystals [49–55], and electric circuit arrays [56–58].

A less explored but equally exciting direction is the exploration of these states in systems lacking translational symmetry, such as quasicrystals. These ideas have recently been explored in two-dimensional (2D) quasicystals [59–65], which require a fine-tuned mass term to generate a higher-order topology. While these initial studies have shed some light on the interplay between aperiodicity and high-order topology, the fine-tuned mass may hinder the realization of higher-order topology in quasicrystals. A common approach to probing the topology in quasicrystals involves examining their higher-dimensional parent systems. For instance, the topology of a one-dimensional (1D) Fibonacci quasicrystal can be elucidated through its mapping to a 2D periodic ancestor in the Harper model, which can be characterized by the Chern number [66–68].

Drawing inspiration from these foundational studies, we shift our focus to a modified Fibonacci quasicrystal, whose higher-dimensional ancestor is the 2D Su-Schrieffer-Heeger (SSH) model [20,69]. The 2D SSH model has several distinct topological phases characterized by the vector Zak phase or, equivalently, Wannier centers, depending on the ratio between intracell hopping γ and intercell hopping γ'. In the nontrivial topological phase of the 2D SSH model, filling anomalies give rise to topological corner states in addition to edge states. By extending the Fibonacci chains to Fibonacci squares, it is possible to explore higher-order topological interfacial states

---

[*] Contact author: donghuixu@cqu.edu.cn

[†] Contact author: ruserzzz@gmail.com

and investigate the preservation of topological properties from high-dimensional parent systems to their lower-dimensional quasicrystal counterparts. Such preservation of topological property cross dimensions without translational symmetry can be verified using artificial structures such as the phononic and photonic quasicrystals, which may offer a hint of the topology of various aperiodic systems.

In this work, we employ the cut-and-project method to construct modified Fibonacci chains and squares from the 2D SSH model. We introduce topological interfaces in these structures, derived from parent systems belonging to different topological classes, and investigate the emergence of topological edge and corner states. The emergence of these interfacial states can be characterized by a shift in the local Wannier center (LWC) spectrum, which indicates filling anomalies in a finite sample. We observe these interfacial states in phononic and photonic quasicrystals through numerical simulations using the finite element method by COMSOL. Our findings suggest that lower-dimensional systems, even in the absence of translational symmetry, can exhibit topological states influenced by the distinct topological classifications of their higher-dimensional periodic ancestors.

The paper is organized as follows. In Sec. II, we introduce the modified Fibonacci chains and the corresponding photonic and phononic quasicrystals whose parent system is the 2D SSH model using the cut-and-project method, and we also introduce the concept of LWC spectrum to characterize the topology in aperiodic systems. In Sec. III, we discuss the topological interfacial states formed in photonic and phononic Fibonacci chains. In Sec. IV, we extend the modified Fibonacci chains to modified Fibonacci squares and explore higher-order topological phases hosting corner states in the phononic and photonic Fibonacci squares. Finally, the discussion and summary are given in Sec. V.

II. CONSTRUCTION OF MODIFIED FIBONACCI CHAINS

The Fibonacci sequence is a sequence in which each number is constructed using a recursive relation $F_n = F_{n-1} + F_{n-2}$. Starting with $F_1 = F_2 = 1$, F_{n-1}/F_{n-2} asymptotically approaches the golden ratio $\tau = (1+\sqrt{5})/2$ as n becomes large. This Fibonacci sequence can be used to construct a 1D quasicrystal, where F_1 and F_2 represent two nonequivalent atomic sites, as denoted by "A" and "B." These two nonequivalent atomic sites differed in the spacing distances and resulting hopping amplitudes, similar to the SSH model [70]. Applying the Fibonacci sequence, we can construct a simple quasicrystal exemplified by an atomic chain such as "ABBABABBABBA...". The tight-binding Hamiltonian of the Fibonacci chain can be written as

$$\mathcal{H} = \sum_n t_n c_{n+1}^\dagger c_n + \text{H.c.}, \tag{1}$$

where $t_n = (t + \lambda V_n)$ denotes the hopping amplitude between site n and $n+1$, $V_n = 2[\lfloor (n+2)/\tau \rfloor) - \lfloor (n+1)/\tau \rfloor)] - 1$ is the characteristic function with $\lfloor x \rfloor$ the floor function, and λ is the hopping difference between A and B sites [66,67,71]. It is noted that the Fibonacci chain can also be obtained using the cut-and-project method from a parent system of higher dimensions, such as a simple 2D square lattice [67].

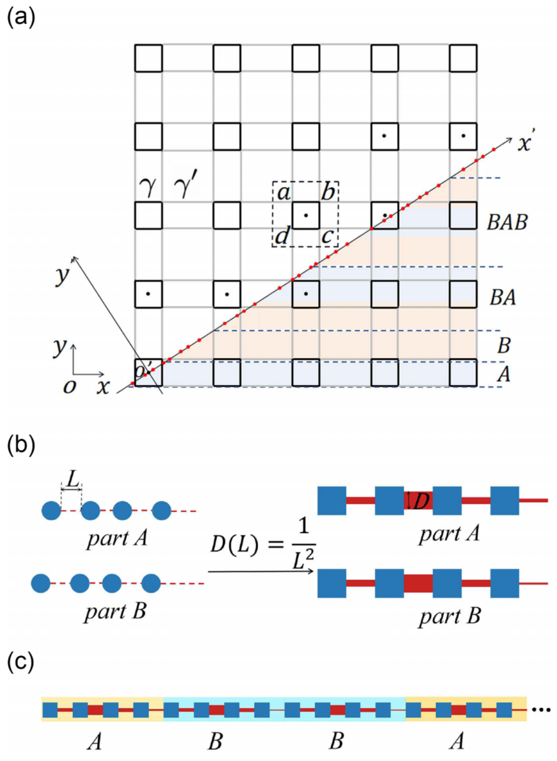

FIG. 1. (a) Schematic of the cut-and-project for the modified Fibonacci chain. The higher-dimensional parent system is the 2D SSH model, which has four sites in one unit cell. When the projection angle is $\tan\theta = 1/\tau$, Fibonacci sequence forms with parts A and B differed by the distances, i.e., $(l+d)\cos\theta$ and $(l+d)\sin\theta$. (b) Parts A and B of the modified Fibonacci chain and the corresponding phononic quasicrystal structure. The modified Fibonacci phononic chain is constructed by mapping the distance between sites to the width of the coupling waveguide as $D(L) = 1/L^2$. (c) Illustration of the modified phononic Fibonacci chain.

In the following, we extend the conventional Fibonacci chain to a modified one through the cut-and-project method. The higher-dimensional parent system is the 2D SSH model, which has several distinct topological phases identified by the Wannier centers and the corresponding vector Zak phase. We expect these modified Fibonacci chains to inherit topological properties, including higher-order ones, from their parent systems. We characterize these topologies by the LWC spectrum and verify this observation through numerical simulations of phononic and photonic quasicrystals.

A. Cut-and-project method

Construction of the Fibonacci chain using the cut-and-project method provides an intuitive understanding of its structure. As illustrated in Fig. 1(a), this method starts with a parent 2D square lattice. The Fibonacci quasicrystal is then generated by projecting these lattice sites onto an axis labeled x'. The orientation of this axis is critical, defined by an angle θ such that $\tan\theta = \omega$ with $\omega = 1/\tau$. The projection strip used for this operation has a width equal to one unit cell of the lattice. As a result, the spacing between the projected centers of the unit cells can have two different values: $(l+d)\cos\theta = (l+d)/\sqrt{1+\omega^2}$ and $(l+d)\sin\theta =$

$(l+d)\omega/\sqrt{1+\omega^2}$. These spacing values correspond to the A and B sites of the Fibonacci chain, as previously mentioned. A modified Fibonacci chain emerges when replacing the simple 2D square lattice with the 2D SSH model in the cut-and-project method.

Before delving into the modified Fibonacci chain, let us quickly review the 2D SSH model first. The 2D SSH model is similar to the 1D case, which has two types of hopping: intracell hopping γ and intercell hopping γ', as illustrated with varying distances and line thicknesses in Fig. 1(a). There are four sublattices in one unit cell, and the hopping amplitudes are alternatively arranged along the x- and y- directions in the 2D SSH model. The topological phases of the 2D SSH model are distinguished by the ratio between $|\gamma/\gamma'|$ and are characterized by the vector Zak phase, or equivalently, by the Wannier center coordinates (ν_x, ν_y). ν_i takes the values within $[0, 1)$ in terms of the lattice constant along the i direction when there is crystalline translational symmetry. For the symmetric case under the point group C_{4v} on which we focus, $\nu_x = \nu_y = 0$ for $\gamma > \gamma'$, and $\nu_x = \nu_y = 1/2$ for $\gamma < \gamma'$ [20]. For $\nu_x = \nu_y = 1/2$, topological edge and corner states emerge.

In the conventional Fibonacci chain, we project every lattice point on the cut axis x'. For the modified Fibonacci chain, we project every four sublattices on the x' axis. The projected unit cells are chosen similarly to that of the conventional Fibonacci chain, which is determined by the projection angle θ. For the modified Fibonacci chain, the projected centers of each unit cell form the Fibonacci sequence, as displayed in Fig. 1(a). The projected positions of these four sublattices in the unit cell (m, n) along the x' axis are given by the following equations:

$$\begin{aligned}
x'_a &= \left(nl+\frac{l}{2}\right)\sin\theta+\left(ml-\frac{l}{2}\right)\cos\theta+md\cos\theta+nd\sin\theta,\\
x'_b &= \left(nl+\frac{l}{2}\right)\sin\theta+\left(ml+\frac{l}{2}\right)\cos\theta+md\cos\theta+nd\sin\theta,\\
x'_c &= \left(nl-\frac{l}{2}\right)\sin\theta+\left(ml+\frac{l}{2}\right)\cos\theta+md\cos\theta+nd\sin\theta,\\
x'_d &= \left(nl-\frac{l}{2}\right)\sin\theta+\left(ml-\frac{l}{2}\right)\cos\theta+md\cos\theta+nd\sin\theta,
\end{aligned} \tag{2}$$

where a, b, c, d are the labels of the sublattices as indicated in Fig. 1(a), l is the distance between sites within a unit cell, and d is the distance between adjacent unit cells with $a = l + d$, the lattice constant of the 2D SSH model.

The unit cell index (m, n) can be picked up by the relation

$$\frac{n-1}{m+1} < \tan\theta \leqslant \frac{n}{m}. \tag{3}$$

It is noted that for $d > l$, there is a possibility that the sublattices of neighboring parts A and B overlap.

B. Modified phononic and photonic Fibonacci quasicrystals

We translate the theoretical framework of the cut-and-project method from the parent 2D SSH model into tangible constructs of phononic and photonic Fibonacci chains. Starting with the photonic quasicrystal, we follow a straightforward method: artificial atoms, such as dielectric rods, are positioned in accordance with the projected sites on the x' from the 2D SSH model as indicated by Eq. (2). This arrangement is depicted in the left panel of Fig. 1(b). In our numerical simulations, we set the radius of the dielectric rod at 0.2 [mm] and the dielectric constant at 100 on an air background. We employ a perfect electric conductor as the boundary condition in the simulation of photonic quasicrystals. Notably, because Maxwell's equations do not have a characteristic length, the size of the photonic quasicrystal can be adjusted without affecting its fundamental properties. The parameters selected here serve illustrative purposes only.

For the phononic quasicrystal, we use square resonators connected by waveguides. The coupling between each resonator is proportional to the width of the waveguides, and we map the distance between the sites to the width of the waveguide as $D = 1/L^n$ with $n = 2$. It should be noted that for other mapping functions, the simulation results remain qualitatively similar. For our simulations, we set the dimensions of each square resonator to 30 [mm] in length, with the waveguides also at a length of 30 [mm]. The uniformity of waveguide length ensures consistent propagation characteristics throughout the phononic quasicrystals. The hard boundary condition is applied in the simulation of phononic quasicrystals. It ensures that the sound pressure is zero at the boundaries, mimicking an isolated system. Figure 1(c) illustrates an example of the modified phononic Fibonacci quasicrystal, where the various shades denote parts A and B.

C. Topology of modified Fibonacci quasicrystals

Here, we discuss how to characterize the topology of the proposed modified Fibonacci chains. Because of the simultaneous presence of time-reversal and inversion symmetries, the Chern number of the proposed system is always zero. Furthermore, because of the lack of discrete translational symmetry, the bulk Wannier center, which corresponds to the Zak phase, is also not well defined. To solve this issue, we propose to use the LWC spectrum to characterize the topology of modified Fibonacci chains and later Fibonacci squares [72,73].

The LWC operator for the unit cell (m, n) can be written as

$$W_{\text{loc}} = \hat{P}\hat{x}_{(m,n)}\hat{P}, \tag{4}$$

where $\hat{P} = \sum_{E\leqslant E_F} |\psi_E\rangle\langle\psi_E|$ is the projection operator for the eigenstates below the occupied energy E_F, and $\hat{x}_{(m,n)} = \sum_x x|x\rangle\langle x|$ is the position operator of summation within the unit cell (m, n). For a finite sample, we define the LWC spectrum at a given E_F as a collection of LWCs for all unit cells defined by Eq. (4).

To obtain an intuitive picture of the LWC spectrum, we display the LWC spectra and eigenspectra for the two topologically distinct cases of the finite-size 2D SSH model in Figs. 2(a) and 2(b) by points blue and orange, respectively. In Fig. 2(a), it is seen that in the trivial case (blue points, $\gamma > \gamma'$), all LWCs stay within the crystalline lattices of the finite sample, while in the nontrivial case (orange points, $\gamma < \gamma'$) partial LWCs jump out of the finite sample range. This is because in the nontrivial case, the number of available LWCs within the sample range shortens due to the nontrivial vector Zak phase

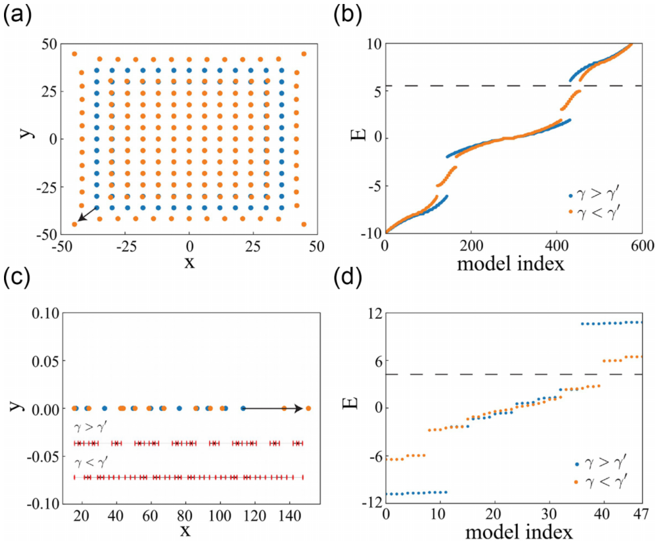

FIG. 2. (a) Local Wannier center spectrum for the two cases of the 2D SSH model for $\gamma > \gamma'$ and $\gamma < \gamma'$. Arrow indicates a local Wannier center shift. (b) Eigenspectra of the cases of the 2D SSH model for $\gamma > \gamma'$ and $\gamma < \gamma'$, where the dashed line indicates the Fermi energy in panel (a). (c) Local Wannier center spectra for the two cases of the modified Fibonacci chains derived from the 2D SSH model for $\gamma > \gamma'$ and $\gamma < \gamma'$. Insets are two schematics of the modified Fibonacci chains, where the line width represents the hopping amplitude. (d) Eigenspectra of the two types of modified Fibonacci chains solved in the tight-binding scheme, where the dashed line indicates the Fermi energy in panel (c).

(π, π), and therefore filling anomalies appear. These filling anomalies manifest as a relative shift in the LCW spectra in Fig. 2(a), as indicated by an arrow from the blue point most outside to the orange point most outside. This LCW shift can be used to characterize the topology of proposed aperiodic systems in the absence of the Chern number. It is noted that, although the LCW seems to be a local quantity, the LCW shift results from all occupied states below the Fermi energy, which cannot be removed by a single defect.

Figure 2(b) displays the eigenspectra of the two cases of the finite-size 2D SSH model used to calculate the LWC spectra in Fig. 2(a), where a dashed line indicates the Fermi energy. We always put E_F in the last gap in the spectrum to avoid missing any possible filling anomaly state, and we can only define the LWC shift in the two systems with the same lattice configuration and size.

In Figs. 2(c) and 2(d), we display the LWC spectra and eigenspectra for the modified Fibonacci chains derived from the two topologically distinct 2D SSH models. The position operator is defined for each A and B part of the Fibonacci chains. As expected, in Fig. 2(c), it appears the LWC shift, which suggests that compared to the modified Fibonacci chain derived from the case of $\gamma > \gamma'$, there are "more" filling anomalies in the modified Fibonacci chain derived from the case of $\gamma < \gamma'$. Considering that the two modified Fibonacci chains have the same lattice configuration, if we put these two cases of modified Fibonacci chains together, interfacial states due to the LWC shift would appear, as demonstrated in later sections. The two modified Fibonacci chains are schematically shown in the inset of Fig. 2(c), where the thickness of the lines represents the hopping amplitude. As seen from the inset, the modified Fibonacci chain of $\gamma < \gamma'$ (nontrivial case in the 2D SSH model) has more isolated sites at the boundaries, consistent with the result of LCW spectra. Figure 2(d) displays the eigenspectra of the two modified Fibonacci chains in a tight-binding model scheme. The Fermi energy is set at the last band gap.

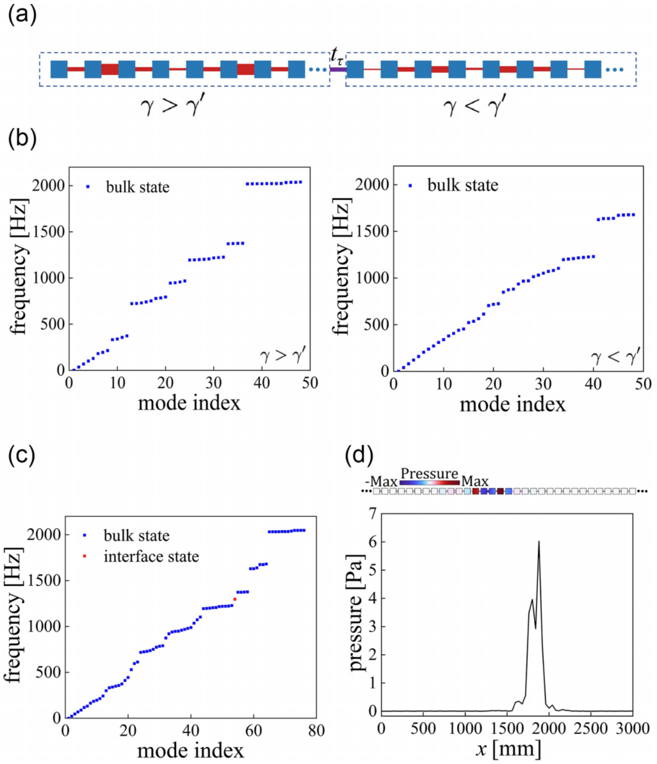

FIG. 3. (a) Topological interface formed by the two types of modified phononic Fibonacci chains, whose higher-dimensional parent systems belonging two topological classes of the 2D SSH model. The coupling between two chains is denoted by t_τ and controlled by the width of the coupling waveguide. (b) Eigenspectra of the two types of modified phononic Fibonacci chains in panel (a), as displayed by left and right panels, respectively. (c) Eigenspectra of the combined structure of the two types of modified phononic Fibonacci chains. (d) Wave profile of the topological interfacial state as sound pressure in the setup of panel (a).

III. TOPOLOGICAL INTERFACIAL STATES

In this section, we delve into topological interfacial states that arise at the junction of two distinct topological systems. We focus on demonstrating the emergence of these topological interfacial states in modified Fibonacci chains derived from phononic and photonic quasicrystals, each with distinct topological characteristics inherited from parent systems. This demonstration is intriguing because, in quasicrystals, the concept of a Wannier center is not well defined because of the absence of translational symmetry, unlike the case of the SSH model.

In addition to demonstrating the emergence of topological interfacial states, symmetry protection of topological states in quasicrystals is also important. Like in the SSH model, chiral symmetry pins the energy of edge states at zero [69].

The role of chiral symmetry in these quasicrystalline systems presents a rich area for exploration, potentially revealing new insights into symmetry protection in topological states. An in-depth investigation of the protection of chiral symmetry in the topological interfacial states of quasicrystals is reserved for future work.

A. Phononic topological interfacial states

We construct a topological interface by joining two phononic Fibonacci chains, each originating from the 2D SSH model but with distinct topological characteristics. This interface, illustrated in Fig. 3(a), is a physical realization of the boundary between different topological phases of the quasicrystals. The left phononic chain is adopted from the 2D SSH model with $l = 1$[mm] and $d = 3$ [mm], effectively resulting in a scenario of $\gamma > \gamma'$. In contrast, the right phononic chain adopts the parameters $l = 3$ [mm] and $d = 1$[mm], which correspond to $\gamma < \gamma'$.

In Fig. 3(b), we display the eigenspectra of the two topologically distinct types of phononic Fibonacci chains derived from the 2D SSH model. There appear multiple gaps in the eigenspectra similar to the conventional Fibonacci chain defined in Eq. (1). The contrast in the eigenspectra of the modified Fibonacci chain is the four subbands in the middle, which reflect the underlying structure of the four sublattices in the 2D SSH model, as displayed by the left panel of Fig. 3(b). In the 2D SSH model, the two different topological phases can be exchanged by redefining the unit cell following a half-period shift. This shift results in a pattern mapping between the two topologically distinct Fibonacci chains, where part A is transformed into part B, and part B becomes BA. However, despite this transformation, parts A and B in the two chains remain nonequivalent due to the different values of l and d, which do not result in the closure of the band gap in their parent systems.

As displayed in Fig. 3(c), we observe the emergence of a topological interfacial state within the shared gap of the two phononic Fibonacci chains. Up to the frequency we solve, there is only one topological interfacial state. By adjusting the coupling strength, denoted as t_τ, between the two chains, we can effectively modulate the frequency of this state within a specific range. This tunability offers a versatile tool for manipulating the properties of the interfacial state for potential applications.

The wave profile of the topological interfacial state, shown in Fig. 3(d), reveals another critical feature: the state exhibits the expected exponential decay along both directions from the interface. This decay is a hallmark of topological interfacial states, indicating the localized nature of these states at the interface of the two distinct topological phases.

The total number of sites in parts A and B of the simulation is 48, corresponding to the Fibonacci sequence "ABBABAB-BABBA." For a larger number of sites, the eigenspectra remain qualitatively the same, and the band gaps do not close.

B. Photonic topological interfacial states

In addition to the phononic Fibonacci chains, it is equally compelling to investigate the topological interfacial states in photonic quasicrystals. One notable aspect of the photonic case is the nonnegligible impact of long-range interactions.

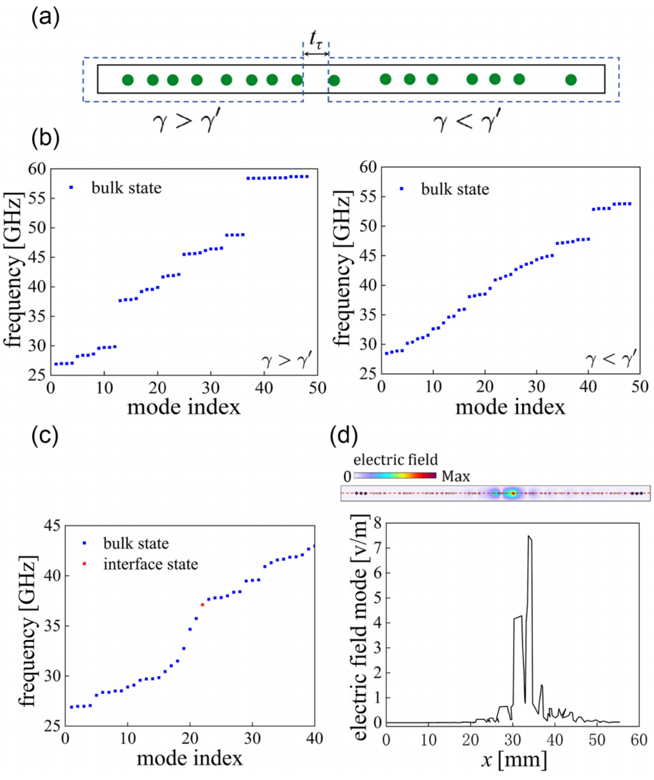

FIG. 4. (a) Topological interface formed by the two types of modified photonic Fibonacci chains, whose higher-dimensional parent systems belonging two topological classes of the 2D SSH model. The coupling between two chains is denoted by t_τ and controlled by the distance between two chains. (b) Eigenspectra of the two types of modified photonic Fibonacci chains in panel (a), as displayed by left and right panels, respectively. (c) Eigenspectra of the combined structure of the two types of modified photonic Fibonacci chains. (d) Wave profile of the topological interfacial state as the electric field in the setup of panel (a).

Figure 4(a) depicts the topological interface between the two distinct types of photonic Fibonacci chains, represented by green points that indicate the placement of the dielectric rods. On examination of the eigenspectra of these photonic chains, as shown in Fig. 4(b), we find a similarity to the phononic case, suggesting similar topological behaviors. The eigenspectra of these two types of photonic Fibonacci chains are displayed in Fig. 4(b), which looks similar to the phononic case. The eigenspectra of the combined structure of these photonic Fibonacci chains, as displayed in Fig. 4(c), reveal a topological interfacial state marked by a red point. Moreover, the wave profile of this topological interfacial state represented as an electric field in photonic Fibonacci chains, is displayed in Fig. 4(d).

IV. HIGHER-ORDER TOPOLOGICAL INTERFACIAL STATES

In Sec. II(A), we introduce the cut-and-project method for constructing modified Fibonacci chains from the 2D SSH model. Building upon this method, we extend its application from constructing Fibonacci chains to Fibonacci squares

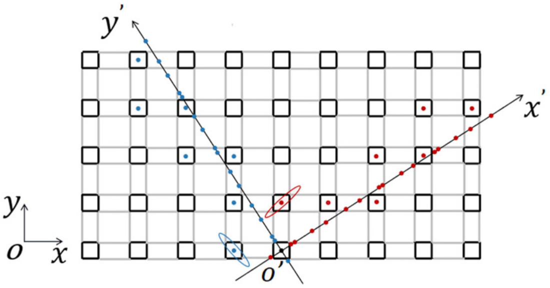

FIG. 5. Schematic of the extended cut-and-project method for the modified Fibonacci square. There are two projecting axes x' and y', whose projection angles are orthogonal. The diagonal sites of the 2D SSH model are projected to the x' axis, and the off-diagonal sites are projected to the y' axis. The red points indicate the site projected on the x' axis, the blue points indicate the site projected on the y' axis.

by delving into studying higher-order topological interfacial states in phononic and photonic quasicrystals.

A. Construction of modified Fibonacci squares

In our quest to construct the Fibonacci square, the traditional chain product method seems somewhat cumbersome. It results in a complex structure with 16 sites in each of parts A and B. We have adapted the cut-and-project method to project sites on both the x' and y' axes to streamline this process. This adaptation involves projecting off-diagonal sites of the 2D SSH model, such as b and d on the x' axis while aligning diagonal sites, namely a and c on the y' axis. The schematic of the extended cut-and-project method for modified Fibonacci squares is depicted in Fig. 5, where there are two projection axes, namely x' and y'. A key aspect of this method is the relationship between the projection angles that satisfies $\theta_{y'} = \theta_{x'} + \pi/2$. This angular arrangement imparts the symmetry of the C_4 point group to the resulting modified Fibonacci square, which simplifies the construction of the corresponding phononic and photonic Fibonacci squares. Coordination of the modified Fibonacci (x'_i, y'_j) is given by

$$\begin{aligned} x'_b &= \left(m_x a + \frac{l}{2}\right)\cos\theta + \left(n_x a + \frac{l}{2}\right)\sin\theta, \\ x'_d &= \left(m_x a - \frac{l}{2}\right)\cos\theta + \left(n_x a - \frac{l}{2}\right)\sin\theta, \\ y'_a &= \left(m_y a - \frac{l}{2}\right)\cos\theta + \left(n_y a + \frac{l}{2}\right)\sin\theta, \\ y'_c &= \left(m_y a + \frac{l}{2}\right)\cos\theta + \left(n_y a - \frac{l}{2}\right)\sin\theta, \end{aligned} \tag{5}$$

where the range of (m_x, n_x), (m_y, n_y) are determined in a similar way as Eq. (3).

B. LWCs of modified Fibonacci squares

Similarly to the case of a modified Fibonacci chain, we can use the LWC spectrum to characterize the filling anomaly in the Fibonacci square. In Fig. 6(a) we display the LWC spectra for the two modified Fibonacci squares derived from the two distinct topological cases of the 2D SSH model. As expected, there appears to be an LWC shift between the two squares. Unlike the 1D case, the $\gamma > \gamma'$ modified Fibonacci square has more filling anomalies than the opposite case. This fact can also be seen from the eigenspectra of the two modified Fibonacci squares in Fig. 6(b), where more localized states emerge in the case of $\gamma > \gamma'$. When inspecting the schematic of the two Fibonacci squares in Fig. 6(c), the invert of filling anomaly in Fig. 6(a) can be owing to the interaction along the second direction. As shown later, when two modified Fibonacci squares are combined, localized interfacial states appear in the $\gamma > \gamma'$ region, consistent with the result of Fig. 6(a).

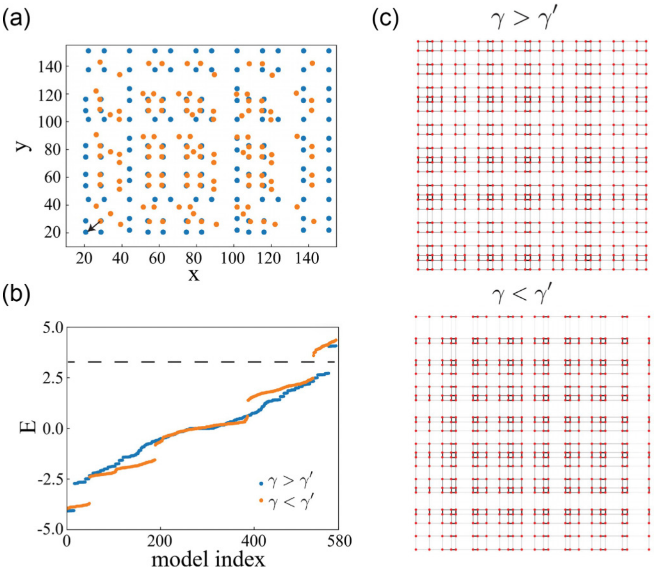

FIG. 6. (a) Local Wannier center spectra of the two cases of modified Fibonacci squares. Arrow indicates a local Wannier center shift. (b) Eigenspectra of the two types of modified Fibonacci squares solved in a tight-binding scheme. The dashed line indicates the Fermi energy in panel (a). (c) Schematics of the two modified Fibonacci squares, where the line width represents the hopping amplitude.

C. Phononic and photonic modified Fibonacci squares

Upon determining the projected positions of the sites on the x' and y' axes, we construct the corresponding modified phononic and photonic Fibonacci squares. Figure 7(a) displays the structures for the two different topological phases in the phononic case. In modified phononic Fibonacci squares, Fibonacci sequences appear along the x and y directions. In the nontrivial phase that $\gamma < \gamma'$, we notice a mix of sites for parts A and B similar to the modified Fibonacci chain. The length of the squares and the coupling waveguide is 5 [mm]. The mapping function between the distance and the width of the coupling waveguide is $D = 1/L^2$.

Figure 7(b) displays the eigenspectra for the modified phononic Fibonacci squares. A common band gap for the two topologically distinct modified Fibonacci squares around 10^4 [Hz] allows us to explore the higher-order topological states.

Turning to the photonic counterpart, Fig. 7(c) illustrates the modified photonic Fibonacci squares, with the left panel representing the $\gamma > \gamma'$ case and the right panel depicting the

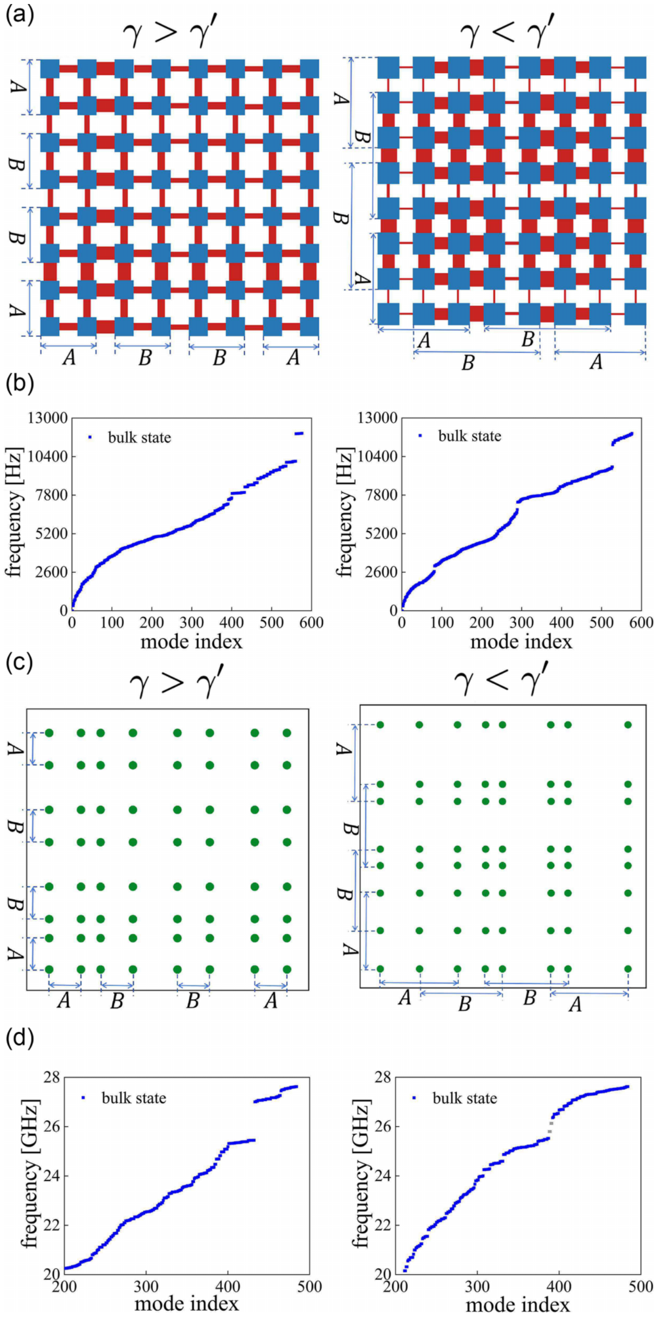

FIG. 7. (a) Schematics of the two types of modified phononic Fibonacci squares, which belongs two topologically distinct classes of the 2D SSH model, constructed by the extended cut-and-project method. (b) Eigenspectra of the two types of modified phononic Fibonacci squares. Left panel is for the case of $\gamma_{\rm intra} > \gamma_{\rm inter}$, and right panel is for $\gamma_{\rm intra} < \gamma_{\rm inter}$. (c) Similar to (a) for the modified photonic Fibonacci squares. (d) Similar to (b) for the modified photonic Fibonacci squares.

opposite case. The radius of the dielectric robs is 0.2 [mm], and the dielectric constant is 100. The remaining part is air. Figure 7(d) displays the eigenspectra of the modified photonic Fibonacci squares. Similarly to the phononic case, we observe a common band gap for both types of squares. In photonic Fibonacci squares, boundary effects lead to the emergence of localized states within the band gap.

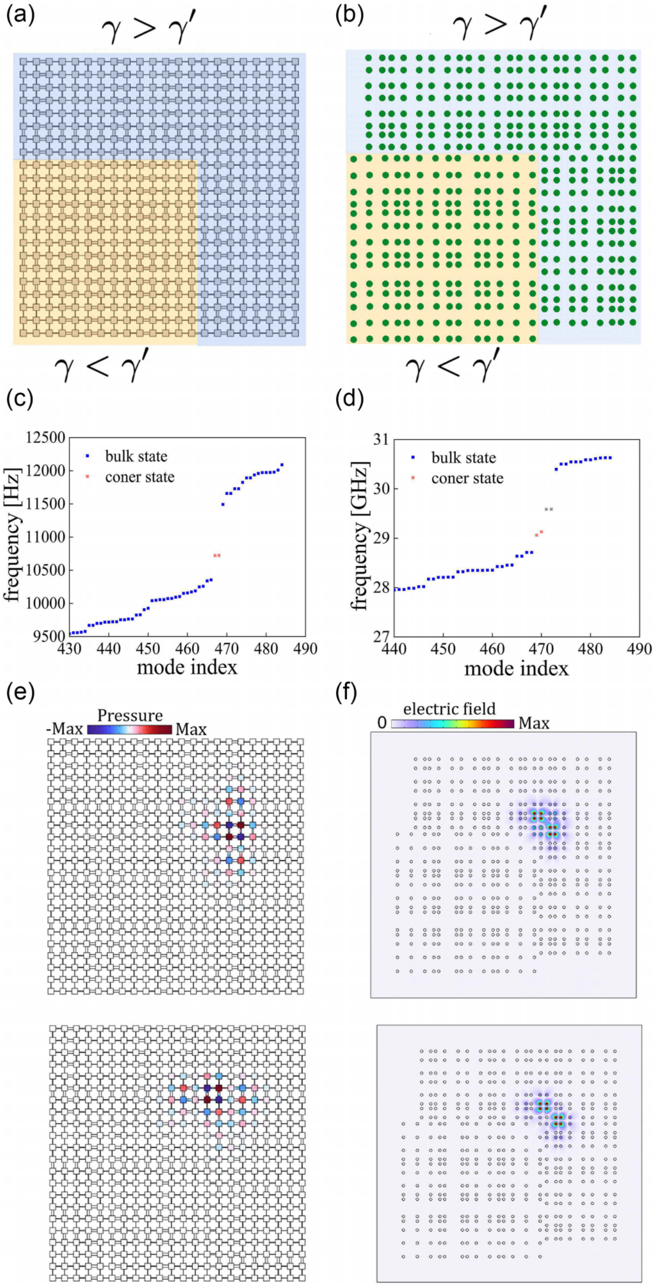

FIG. 8. (a) Topological interface with a corner structure formed by two types of modified phononic Fibonacci squares. (b) Topological interface with a corner structure formed by two types of modified photonic Fibonacci squares. (c) Eigenspectra for the combined structure in panel (a). (d) Eigenspectra for the combined structure in panel (b). (e) Wave profiles as sound pressure of the topological corner states in panel (c). (f) Wave profiles as electric fields of the topological corner states in panel (d).

D. Corner states in modified Fibonacci squares

We demonstrate that topological corner states emerge when combining two distinct types of modified Fibonacci squares. The combined modified phononic and photonic Fibonacci square setup are displayed in Figs. 8(a) and 8(b), respectively. The different shades indicate their topological classifications. A corner structure is constructed in the combined phononic and photonic Fibonacci squares in each setup.

The eigenspectra of these combined structures for the phononic and photonic cases are displayed in Figs. 8(c) and 8(d) with zooming in around the last band gap. A notable observation is the appearance of corner states within the common band gaps of these configurations. Interestingly, these corner states exhibit double degeneracy, distinguishing them from the topological interfacial states observed in the modified Fibonacci chain. This characteristic is further elucidated in the wave profiles of the corner states for both the phononic and photonic cases, shown in Figs. 8(e) and 8(f). Here, we observe that, unlike the corner states typically seen in the 2D SSH model, which are localized at the corner sites, the corner states in our modified Fibonacci square model manifest around the corner sites rather than directly at them. This unique localization pattern of the corner states in our model provides new insights into the behavior of topological states in quasicrystalline systems. It contributes to our understanding of their topological characteristics.

V. SUMMARY

In summary, we have proposed a modified Fibonacci quasicrystal whose higher-dimensional parent system is the two-dimensional Su-Schrieffer-Heeger model. By constructing the corresponding phononic and photonic quasicrystals of the modified Fibonacci chains and squares, we observe that topological interfacial states including higher-order ones such as corner states that emerge in the finite-element simulations. Our results suggest that, in addition to the Chern-insulator states, higher-order topological states induced by filling anomalies can also be inherited from the parent systems in quasicrystals. The discussed phononic and photonic quasicrystals of modified Fibonacci quasicrystals offer a platform for further study of the higher-order topological properties in quasicrystals.

ACKNOWLEDGMENTS

F.L. thanks Rui Chen for the useful discussion. This work is supported by the NSFC under Grants No. 12074205, No. 12074108, and No. 12347101, the NSFZP under Grant No. LQ21A040004, the Natural Science Foundation of Chongqing under Grant No. CSTB2022NSCQ-MSX0568, and the Fundamental Research Funds for the Central Universities under Grant No. 2023CDJXY-048.

[1] M. Z. Hasan and C. L. Kane, Colloquium: Topological insulators, Rev. Mod. Phys. **82**, 3045 (2010).
[2] X.-L. Qi and S.-C. Zhang, Topological insulators and superconductors, Rev. Mod. Phys. **83**, 1057 (2011).
[3] A. Bansil, H. Lin, and T. Das, Colloquium: Topological band theory, Rev. Mod. Phys. **88**, 021004 (2016).
[4] Y. Hatsugai, Chern number and edge states in the integer quantum Hall effect, Phys. Rev. Lett. **71**, 3697 (1993).
[5] L. Fu and C. L. Kane, Time reversal polarization and a Z_2 adiabatic spin pump, Phys. Rev. B **74**, 195312 (2006).
[6] Y. Hwang, J. Ahn, and B.-J. Yang, Fragile topology protected by inversion symmetry: Diagnosis, bulk-boundary correspondence, and Wilson loop, Phys. Rev. B **100**, 205126 (2019).
[7] A. Bouhon, A. M. Black-Schaffer, and R.-J. Slager, Wilson loop approach to fragile topology of split elementary band representations and topological crystalline insulators with time-reversal symmetry, Phys. Rev. B **100**, 195135 (2019).
[8] Z. Wang, L. Dong, C. Xiao, and Q. Niu, Berry curvature effects on quasiparticle dynamics in superconductors, Phys. Rev. Lett. **126**, 187001 (2021).
[9] G. Harari, M. A. Bandres, Y. Lumer, M. C. Rechtsman, Y. D. Chong, M. Khajavikhan, D. N. Christodoulides, and M. Segev, Topological insulator laser: Theory, Science **359**, eaar4003 (2018).
[10] M. Ezawa, Topological switch between second-order topological insulators and topological crystalline insulators, Phys. Rev. Lett. **121**, 116801 (2018).
[11] W. A. Benalcazar, T. Li, and T. L. Hughes, Quantization of fractional corner charge in C_n-symmetric higher-order topological crystalline insulators, Phys. Rev. B **99**, 245151 (2019).
[12] Y. Wu, H. Jiang, J. Liu, H. Liu, and X. C. Xie, Non-Abelian braiding of Dirac fermionic modes using topological corner states in higher-order topological insulator, Phys. Rev. Lett. **125**, 036801 (2020).
[13] H. Watanabe and H. C. Po, Fractional corner charge of sodium chloride, Phys. Rev. X **11**, 041064 (2021).
[14] M. Jung, Y. Yu, and G. Shvets, Exact higher-order bulk-boundary correspondence of corner-localized states, Phys. Rev. B **104**, 195437 (2021).
[15] S.-B. Zhang, W. B. Rui, A. Calzona, S.-J. Choi, A. P. Schnyder, and B. Trauzettel, Topological and holonomic quantum computation based on second-order topological superconductors, Phys. Rev. Res. **2**, 043025 (2020).
[16] S.-B. Zhang, A. Calzona, and B. Trauzettel, All-electrically tunable networks of Majorana bound states, Phys. Rev. B **102**, 100503(R) (2020).
[17] T. E. Pahomi, M. Sigrist, and A. A. Soluyanov, Braiding Majorana corner modes in a second-order topological superconductor, Phys. Rev. Res. **2**, 032068(R) (2020).
[18] X.-H. Pan, X.-J. Luo, J.-H. Gao, and X. Liu, Detecting and braiding higher-order Majorana corner states through their spin degree of freedom, Phys. Rev. B **105**, 195106 (2022).
[19] S. Tang, Y. Xu, F. Ding, and F. Liu, Continuously tunable topological defects and topological edge states in dielectric photonic crystals, Phys. Rev. B **107**, L041403 (2023).
[20] F. Liu and K. Wakabayashi, Novel topological phase with a zero berry curvature, Phys. Rev. Lett. **118**, 076803 (2017).
[21] W. A. Benalcazar, B. A. Bernevig, and T. L. Hughes, Quantized electric multipole insulators, Science **357**, 61 (2017).
[22] W. A. Benalcazar, B. A. Bernevig, and T. L. Hughes, Electric multipole moments, topological multipole moment pumping, and chiral hinge states in crystalline insulators, Phys. Rev. B **96**, 245115 (2017).

[23] M. Ezawa, Higher-order topological insulators and semimetals on the breathing kagome and pyrochlore lattices, Phys. Rev. Lett. **120**, 026801 (2018).
[24] F. Liu, H.-Y. Deng, and K. Wakabayashi, Helical topological edge states in a quadrupole phase, Phys. Rev. Lett. **122**, 086804 (2019).
[25] L. Trifunovic and P. W. Brouwer, Higher-order bulk-boundary correspondence for topological crystalline phases, Phys. Rev. X **9**, 011012 (2019).
[26] E. Khalaf, W. A. Benalcazar, T. L. Hughes, and R. Queiroz, Boundary-obstructed topological phases, Phys. Rev. Res. **3**, 013239 (2021).
[27] Z. Lei, Y. Deng, and L. Li, Topological classification of Higher-order topological phases with nested band inversion surfaces, Phys. Rev. B **106**, 245105 (2022).
[28] W. Jia, X.-C. Zhou, L. Zhang, L. Zhang, and X.-J. Liu, Unified characterization for higher-order topological phase transitions, Phys. Rev. Res. **5**, L022032 (2023)
[29] S. Saha, T. Nag, and S. Mandal, Multiple higher-order topological phases with even and odd pairs of zero-energy corner modes in a C_3symmetry broken model, Europhys. Lett. **142**, 56002 (2023).
[30] Z. Song, Z. Fang, and C. Fang, $(d-2)$-dimensional edge states of rotation symmetry protected topological states, Phys. Rev. Lett. **119**, 246402 (2017).
[31] J. Langbehn, Y. Peng, L. Trifunovic, F. von Oppen, and P. W. Brouwer, Reflection-symmetric second-order topological insulators and superconductors, Phys. Rev. Lett. **119**, 246401 (2017).
[32] M. Geier, L. Trifunovic, M. Hoskam, and P. W. Brouwer, Second-order topological insulators and superconductors with an order-two crystalline symmetry, Phys. Rev. B **97**, 205135 (2018).
[33] E. Khalaf, Higher-order topological insulators and superconductors protected by inversion symmetry, Phys. Rev. B **97**, 205136 (2018).
[34] R. Okugawa, S. Hayashi, and T. Nakanishi, Second-order topological phases protected by chiral symmetry, Phys. Rev. B **100**, 235302 (2019).
[35] W. A. Benalcazar and A. Cerjan, Chiral-symmetric higher-order topological phases of matter, Phys. Rev. Lett. **128**, 127601 (2022).
[36] F. Schindler, A. M. Cook, M. G. Vergniory, Z. Wang, S. S. P. Parkin, B. A. Bernevig, and T. Neupert, Higher-order topological insulators, Sci. Adv. **4**, eaat0346 (2018).
[37] F. Schindler, Z. Wang, M. G. Vergniory, A. M. Cook, A. Murani, S. Sengupta, A. Y. Kasumov, R. Deblock, S. Jeon, I. Drozdov, H. Bouchiat, S. Guéron, A. Yazdani, B. A. Bernevig, and T. Neupert, Higher-order topology in bismuth, Nat. Phys. **14**, 918 (2018).
[38] C. Yue, Y. Xu, Z. Song, H. Weng, Y.-M. Lu, C. Fang, and X. Dai, Symmetry-enforced chiral hinge states and surface quantum anomalous Hall effect in the magnetic axion insulator $Bi_{2-x}Sm_xSe_3$, Nat. Phys. **15**, 577 (2019).
[39] B. Liu, G. Zhao, Z. Liu, and Z. F. Wang, Two-dimensional quadrupole topological insulator in γ-graphyne, Nano Lett. **19**, 6492 (2019).
[40] Y.-B. Choi, Y. Xie, C.-Z. Chen, J. Park, S.-B. Song, J. Yoon, B. J. Kim, T. Taniguchi, K. Watanabe, J. Kim, K. C. Fong, M. N. Ali, K. T. Law, and G.-H. Lee, Evidence of higher-order topology in multilayer WTe_2 from Josephson coupling through anisotropic hinge states, Nat. Mater. **19**, 974 (2020).
[41] L. Aggarwal, P. Zhu, T. L. Hughes, and V. Madhavan, Evidence for higher-order topology in Bi and $Bi_{0.92}Sb_{0.08}$, Nat. Commun. **12**, 4420 (2021).
[42] R.-X. Zhang, W. S. Cole, X. Wu, and S. Das Sarma, Higher-order topology and nodal topological superconductivity in Fe(Se,Te) heterostructures, Phys. Rev. Lett. **123**, 167001 (2019).
[43] B.-Y. Xie, H.-F. Wang, H.-X. Wang, X.-Y. Zhu, J.-H. Jiang, M.-H. Lu, and Y.-F. Chen, Second-order photonic topological insulator with corner states, Phys. Rev. B **98**, 205147 (2018).
[44] B.-Y. Xie, G.-X. Su, H.-F. Wang, H. Su, X.-P. Shen, P. Zhan, M.-H. Lu, Z.-L. Wang, and Y.-F. Chen, Visualization of higher-order topological insulating phases in two-dimensional dielectric photonic crystals, Phys. Rev. Lett. **122**, 233903 (2019).
[45] X.-D. Chen, W.-M. Deng, F.-L. Shi, F.-L. Zhao, M. Chen, and J.-W. Dong, Direct observation of corner states in second-order topological photonic crystal slabs, Phys. Rev. Lett. **122**, 233902 (2019).
[46] S. Mittal, V. V. Orre, G. Zhu, M. A. Gorlach, A. Poddubny, and M. Hafezi, Photonic quadrupole topological phases, Nat. Photon. **13**, 692 (2019).
[47] A. Cerjan, M. Jürgensen, W. A. Benalcazar, S. Mukherjee, and M. C. Rechtsman, Observation of a higher-order topological bound state in the continuum, Phys. Rev. Lett. **125**, 213901 (2020).
[48] Y. Wang, Y. Ke, Y.-J. Chang, Y.-H. Lu, J. Gao, C. Lee, and X.-M. Jin, Constructing higher-order topological states in higher dimensions, Phys. Rev. B **104**, 224303 (2021).
[49] M. Serra-Garcia, V. Peri, R. Süsstrunk, O. R. Bilal, T. Larsen, L. G. Villanueva, and S. D. Huber, Observation of a phononic quadrupole topological insulator, Nature (London) **555**, 342 (2018).
[50] H. Xue, Y. Yang, F. Gao, Y. Chong, and B. Zhang, Acoustic higher-order topological insulator on a kagome lattice, Nat. Mater. **18**, 108 (2019).
[51] H. Xue, Y. Yang, G. Liu, F. Gao, Y. Chong, and B. Zhang, Realization of an acoustic third-order topological insulator, Phys. Rev. Lett. **122**, 244301 (2019).
[52] R.-X. Zhang, W. S. Cole, and S. Das Sarma, Helical hinge Majorana modes in iron-based superconductors, Phys. Rev. Lett. **122**, 187001 (2019).
[53] X. Zhang, H.-X. Wang, Z.-K. Lin, Y. Tian, B. Xie, M.-H. Lu, Y.-F. Chen, and J.-H. Jiang, Second-order topology and multidimensional topological transitions in sonic crystals, Nat. Phys. **15**, 582 (2019).
[54] Z.-K. Lin, H.-X. Wang, Z. Xiong, M.-H. Lu, and J.-H. Jiang, Anomalous quadrupole topological insulators in two-dimensional nonsymmorphic sonic crystals, Phys. Rev. B **102**, 035105 (2020).
[55] Z.-K. Lin, S.-Q. Wu, H.-X. Wang, and J.-H. Jiang, Higher-order topological spin Hall effect of sound, Chin. Phys. Lett. **37**, 074302 (2020).
[56] S. Imhof, C. Berger, F. Bayer, J. Brehm, L. W. Molenkamp, T. Kiessling, F. Schindler, C. H. Lee, M. Greiter, T. Neupert, and R. Thomale, Topolectrical-circuit realization of topological corner modes, Nat. Phys. **14**, 925 (2018).

[57] S. Liu, S. Ma, Q. Zhang, L. Zhang, C. Yang, O. You, W. Gao, Y. Xiang, T. J. Cui, and S. Zhang, Octupole corner state in a three-dimensional topological circuit, Light Sci. Appl. **9**, 145 (2020).

[58] Z. Wang, X.-T. Zeng, Y. Biao, Z. Yan, and R. Yu, Realization of a Hopf insulator in circuit systems, Phys. Rev. Lett. **130**, 057201 (2023).

[59] R. Chen, C.-Z. Chen, J.-H. Gao, B. Zhou, and D.-H. Xu, Higher-order topological insulators in quasicrystals, Phys. Rev. Lett. **124**, 036803 (2020).

[60] D. Varjas, A. Lau, K. Pöyhönen, A. R. Akhmerov, D. I. Pikulin, and I. C. Fulga, Topological phases without crystalline counterparts, Phys. Rev. Lett. **123**, 196401 (2019).

[61] C.-B. Hua, R. Chen, B. Zhou, and D.-H. Xu, Higher-order topological insulator in a dodecagonal quasicrystal, Phys. Rev. B **102**, 241102(R) (2020).

[62] S. Spurrier and N. R. Cooper, Kane-mele with a twist: Quasicrystalline higher-order topological insulators with fractional mass kinks, Phys. Rev. Res. **2**, 033071 (2020).

[63] L. Huang, W. Zhang, and X. Zhang, Moiré quasibound states in the continuum, Phys. Rev. Lett. **128**, 253901 (2022).

[64] C. Wang, F. Liu, and H. Huang, Effective model for fractional topological corner modes in quasicrystals, Phys. Rev. Lett. **129**, 056403 (2022).

[65] R. Chen, C.-B. Hua, H.-P. Sun, and B. Zhou, Finite-size effect on quantum percolation in topological insulators, J. Phys.: Condens. Matter **36**, 125001 (2024).

[66] Y. E. Kraus and O. Zilberberg, Topological equivalence between the Fibonacci quasicrystal and the Harper model, Phys. Rev. Lett. **109**, 116404 (2012).

[67] A. Jagannathan, The fibonacci quasicrystal: Case study of hidden dimensions and multifractality, Rev. Mod. Phys. **93**, 045001 (2021).

[68] A. Panigrahi, V. Juričić, and B. Roy, Projected topological branes, Commun. Phys. **5**, 230 (2022).

[69] F. Liu, Analytic solution of the n-dimensional Su-Schrieffer-Heeger model, Phys. Rev. B **108**, 245140 (2023).

[70] W. P. Su, J. R. Schrieffer, and A. J. Heeger, Solitons in polyacetylene, Phys. Rev. Lett. **42**, 1698 (1979).

[71] H. Au-Yang and J. H. H. Perk, Q-dependent susceptibilities in ferromagnetic quasiperiodic z-invariant Ising models, J. Stat. Phys. **127**, 265 (2007).

[72] J. Sykes and R. Barnett, Local topological markers in odd dimensions, Phys. Rev. B **103**, 155134 (2021).

[73] J. Sykes and R. Barnett, 1D quasicrystals and topological markers, Mater. Quantum Technol. **2**, 025005 (2022).